Nanoscale

Accepted Manuscript

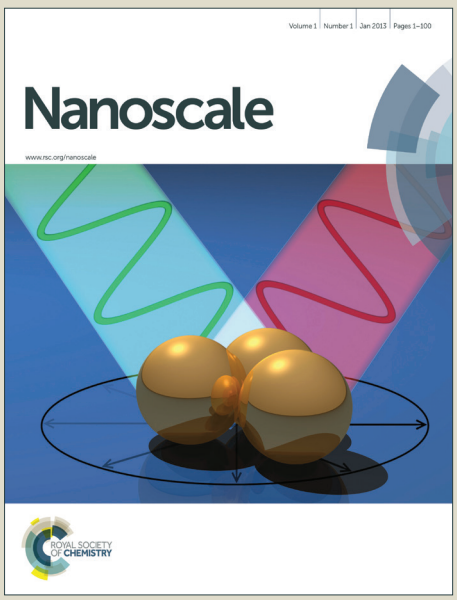

ROYAL SOCIETY OF CHEMISTRY

www.rsc.org/nanoscale

Nanoscale

RSCPublishing

COMMUNICATION

Electrospun manganese-cobalt oxide hollow nanofibres synthesized via combustion reactions and their lithium storage performance†

Soo Min Hwang,‡§[a] So Yeun Kim,‡[bc] Jae-Geun Kim,[b] Ki Jae Kim,[b] Jong-Won Lee,[d] Min-Sik Park,*[b] Young-Jun Kim,[b] Mohammed Shahabuddin,[e] Yusuke Yamauchi[f] and Jung Ho Kim*[a]

Cite this: DOI: 10.1039/xoxxoooooox

Received ooth January 2015,
Accepted ooth January 2015

DOI: 10.1039/xoxxoooooox

www.rsc.org/

Mesoporous hollow fibres of $MnCo_2O_4$ and $CoMn_2O_4$ were synthesized by electrospinning and highly exothermic oxygen-mediated combustion reactions during calcination, in which the heating rate affected the final fibre morphology (e.g., single- or double-shell). The anodes consisting of the hollow fibres showed excellent electrochemical properties for lithium-ion batteries.

Hollow porous nanostructured materials (HPNMs) have been recognised as effective building blocks in a variety of scientific and engineering applications, such as sensors, catalysts, and electrochemical energy conversion and storage devices.[1-5] Owing to their structures featuring high porosity and a large surface-to-volume ratio, HPNMs can provide sufficient active sites for physicochemical reactions with their surroundings, ensuring high sensitivity (activity) and superior kinetics (efficiency).[6-9] Recently, mixed transition-metal oxides (MTMOs), such as single-phase ternary metal oxides with two different metal cations, typically in a spinel structure of $A_xB_{3-x}O_4$, where A and B can be Co, Ni, Mn, Zn, Fe, etc., have captured much attention as promising electrode materials in electrochemical energy conversion and storage systems.[10] These MTMOs exhibit high electrochemical activity originating from their complex chemical compositions, as well as higher electrical conductivity than simple TMOs due to the relatively low activation energy for electron transfer between cations.[10] Utilising MTMOs with hollow/porous architectures thus would match with the recent trend towards both high energy density and high power density in the electrochemical energy conversion/storage field, as a result of enhanced near-surface storage capacity and activity.[11] Up to now, various forms of cobalt- or manganese-based MTMO nanostructures have been studied intensively as promising electrode materials for advanced lithium batteries and electrochemical capacitors, as well as electrocatalysts for oxygen reduction/evolution reactions.[10,12-15] Fibrous manganese-cobalt oxide hollow nanostructures, however, have been rarely reported.[16] Herein, we report mesoporous hollow nanofibres of $MnCo_2O_4$ (MCO) and $CoMn_2O_4$ (CMO) that were fabricated by using a facile electrospinning route and highly exothermic combustion reactions during calcination in air. The formation pathway of the synthesized fibrous tubular structures was found to be different from the existing heterogeneous contraction mechanism which affects the final morphology of hollow structures, depending on the ramping rate during heat-treatment.[13,17] The resulting electrospun hollow MCO and CMO fibres displayed excellent lithium storage capacity, and good cycling performance and rate capability as lithium-ion battery (LIB) anodes.

First, in order to prepare the precursor solutions for electrospinning, cobalt- and manganese-acetate powders with a molar ratio of 2:1 and 1:2 for MCO and CMO samples, respectively, were dissolved in N,N-dimethylformamide and then poly-vinylpyrrolidone (PVP) was added under magnetic stirring. The resulting transparent solutions were subjected to an electrospinning process, dried at 150 ^oC, and heat-treated at 600 ^oC in ambient air. The specific synthesis conditions can be found in the 'Experimental section' in the electronic supplementary information (ESI†).

The morphology of the electrospun MCO and CMO fibres was observed by field-emission scanning electron microscopy (FESEM) (Fig. 1). The as-dried mats of the MCO and CMO fibres (Fig. 1a and b) exhibited typical reticular morphologies where the individual fibres had smooth surface (see the corresponding insets). After calcination at 600 ^oC (with a heating rate of 5 ^oC/min), both the samples (Fig. 1c and d) possessed fibre lengths of a few hundred micrometers and average diameters of 185 nm (MCO) and 162 nm (CMO) (Fig. S1†), and they showed particulate surfaces, as displayed in the high-magnification FESEM images (insets of Fig. 1c and d). Notably, it was observed that the CMO sample had a rougher surface morphology than the MCO sample and discernible pores with a size of 30-70 nm. In addition, from the images of the fractured fibres of both the samples (Fig. 1e and f), we found that the fibres had a hollow structure. The MCO and CMO samples belonged to a face-centred-cubic spinel $MnCo_2O_4$ phase (space group Fd3m (227), JCPDS No. 23-1237) and a body-centred tetragonal spinel $CoMn_2O_4$ phase (space group $I4_1/amd$, JCPDS No. 77-0471), respectively, without any notable impurity phase (Fig. S2a and c†).

In order to probe the formation mechanism of the hollow fibres, we performed thermogravimetric and differential thermal analyses

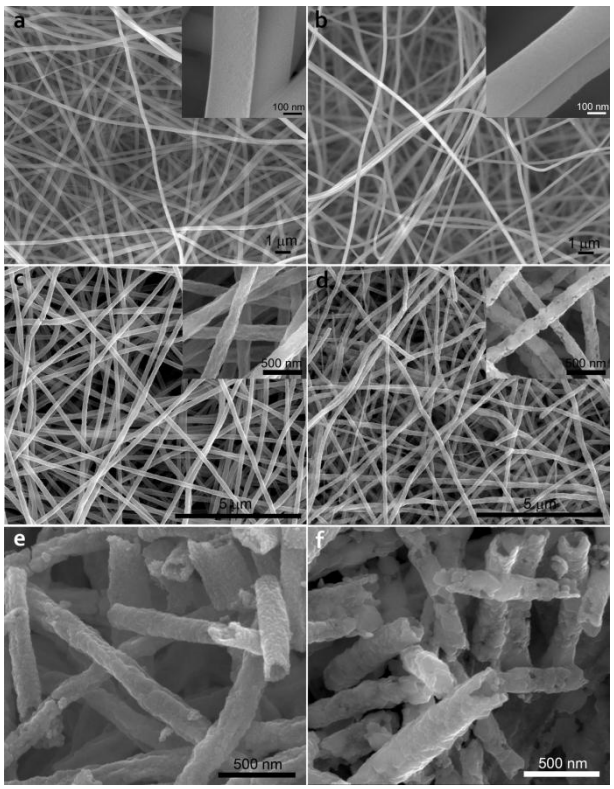

Fig. 1 SEM images of (a, b) as-dried and (c-f) annealed MCO (a, c, e) and CMO (b, d, f) fibres. The insets in (a-d) show magnified images of the corresponding fibres.

(TG/DTA) on the as-dried MCO and CMO fibres. As demonstrated in Fig. 2, the TG curves of both the samples commonly showed a gentle decrease until around 200 °C, followed by an abrupt weight loss, which was accompanied by a highly exothermic reaction in the DTA. Note the abnormal shapes in the TG and DTA curves, i.e., the loop-like shapes, implying that the heat generated from the sample

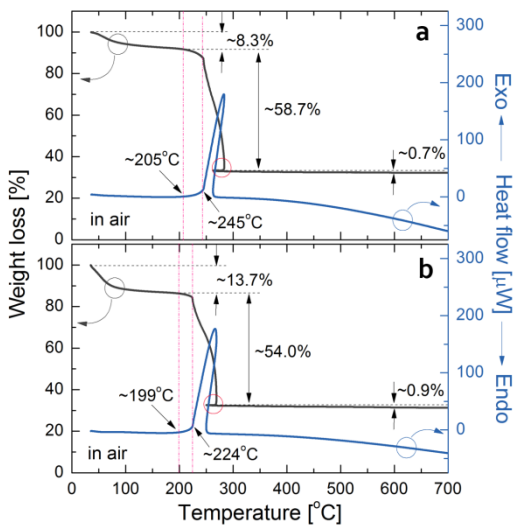

Fig. 2 TG/DTA curves of as-dried (a) MCO and (b) CMO fibres. The ramping rate was 5 °C/min. The abnormal shaped regions marked by red circles reveal the occurrence of highly exothermic reactions during the calcination.

increased the temperature at the sample crucible faster than the programmed heating rate of 5 °C/min (refer to Fig. S3a†).[18] Afterwards, negligible weight loss was found up to 700 °C for both the samples, which indicates complete decomposition of the organic components within the as-dried electrospun fibres below around 250 °C. Interestingly, no notable exothermic peak in the DTA data under N_2 atmosphere was detected (Fig. S3b†). Thus, the strongly exothermic peaks possibly originated from reactions between the ambient oxygen and the organics decomposed from PVP and –acetate groups of the gel-state fibres during calcination.[18,19] It has been reported that hollow nanostructures can evolve by a particular pathway, so-called '*heterogeneous contraction*,' during heat-treatment, based on a non-equilibrium heat-treatment condition, in which the heating rate (*R*) significantly affects the final geometry; increasing *R* ordinarily results in hollow structures and further high complexity, such as double-wall or triple-wall structures.[13,17]

Keeping the high dependence on *R* of the heterogeneous contraction mechanism in mind, we compared the morphology and elemental distributions of MCO and CMO fibres that experienced different conditions of *R* (0.5 °C/min vs. 5 °C/min) during calcination. Interestingly, the electrospun MCO and CMO samples, herein, exhibited the opposite behaviour to existing heterogeneous contraction with respect to the formation of hollow structures: even the slow *R* (at 0.5 °C/min) generated hollow morphology and high complexity, such as double-wall tubes. For example, the MCO

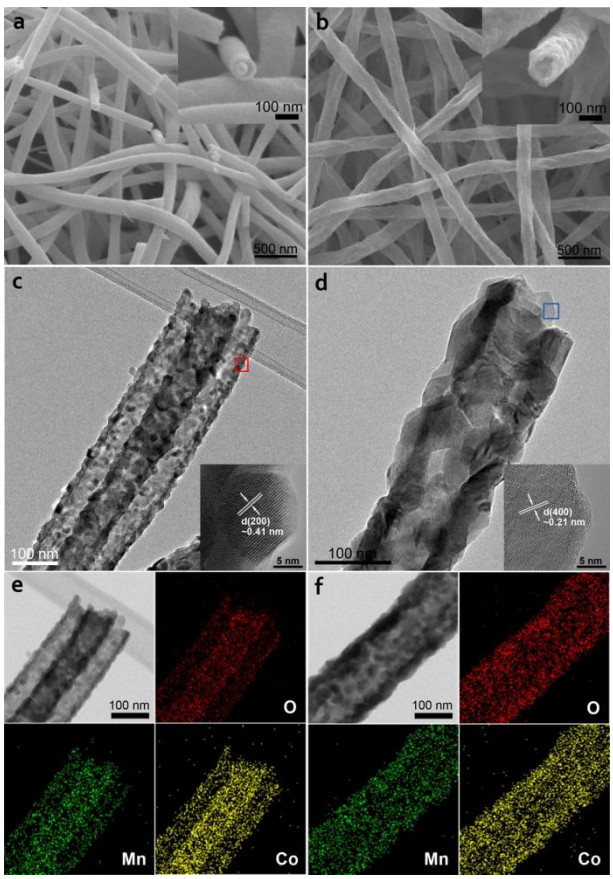

Fig. 3 (a, b) SEM, (c, d) TEM, and (e, f) EDS mapping images of MCO fibres annealed at different heating rates of 0.5 °C/min (a, c, e) and 5 °C/min (b, d, f). The insets in (a) and (b) show cross-sectional images of representative hollow fibres, and those in (c) and (d) are HRTEM images of the regions marked by squares; (e) and (f) present the elemental distributions of O, Mn, and Co.

sample subjected to heating at a an *R* value of 0.5 °C/min, hereafter denoted as MCO-0.5 (Fig. 3a), had double-wall hollow structures and relatively smooth surfaces, compared to its counterpart at 5 °C/min, denoted as MCO-5 (Fig. 3b). From the transmission electron microscope (TEM) images, the double-wall tubular morphology with small particle sizes was clearly observed for MCO-0.5 (Fig. 3c), whereas the MCO-5 featured a single-wall hollow structure with large particle sizes, and hence, relatively rough surface morphology (Fig. 3d). Both the samples commonly had a cubic spinel $MnCo_2O_4$ phase (refer to the XRD patterns in Fig. S2a and b†); the interplanar distance (*d*) of the lattice fringes was measured to be ~0.41 nm and ~0.21 nm for MCO-0.5 and MCO-5, respectively, corresponding to (200) and (400) planes of the $MnCo_2O_4$ phase (insets in Fig. 3c and d and the corresponding fast-Fourier transform (FFT) patterns in Fig. S4†). The EDS mapping (Fig. 3e and f) displays the uniform distribution of O, Mn, and Co elements, and overall, the ratio of Co to Mn was evaluated to be ~2.1 and ~2.0 for MCO-0.5 and MCO-5, respectively.

In the same manner, the CMO fibres annealed at *R* of 0.5 °C/min (CMO-0.5) showed smooth surface morphology and hollow structures with high complexity, such as core-in-tube, together with single-wall hollow structures (refer to Fig. S5†). Interestingly, the non-uniform fibres with large grains were often observed, probably due to the abnormal grain growth (Fig. S6†). Generally, the grain growth in spinel oxide phases is affected by the chemical composition.[20] It has been reported that a higher proportion of Mn element results in an increased grain growth rate in cobalt-based spinel oxides, due to the faster migration rate of Mn cations than Co cations in the O anion array,[21] which is thus considered to be responsible for the formation of the peculiar-shaped CMO fibres with relatively large grains.

The porosity of the MCO and CMO fibres was evaluated by N_2 sorption isotherm measurements (Fig. S7†). All the samples featured mesoporosity with a type IV isotherm characteristic.[22] The average pore size (D_{pore}), total pore volume (V_{pore}), and Brunauer-Emmett-Teller (BET) surface area (S_{BET}) are summarized in Table 1. It was found that the MCO samples were a little more porous than the CMO samples, which was probably due to the aforementioned difference in migration rates of cationic elements and thereby different grain growth behaviours during calcination, although the porosity of the samples was less dependent on *R* during calcination.

Based on the above thermal analyses and structural investigation, the formation pathways of single- and double-wall hollow fibres via combustion reactions are schematically illustrated in Fig. 4. The calcination in ambient air could allow the gel-state fibres, which mainly consist of metal-acetate (M-Ac) and PVP, to be subjected to two different types of forces in opposite directions (top left). The inward force (σ_i) possibly originates from contraction (volume loss) by pyrolysis of the organic components of the fibres during

Table 1 Average pore size (D_{pore}), total pore volume (V_{pore}), and Brunauer-Emmett-Teller (BET) surface area (S_{BET}) of MCO and CMO fibres subjected to different heating rates of 0.5 °C/min and 5 °C/min. All the samples showed mesoporosity and similar D_{pore}.

Sample	D_{pore} [nm]	V_{pore} [cm^3/g]	S_{BET} [m^2/g]
MCO-0.5	23.1	0.112	19.3
MCO-5	21.1	0.102	19.3
CMO-0.5	16.0	0.040	10.1
CMO-5	19.4	0.078	16.0

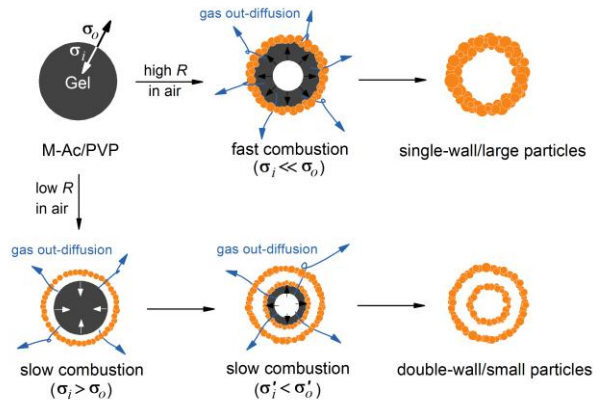

Fig. 4 Schematic illustration showing the formation process of single- and double-wall hollow fibres via combustion reactions. During calcination under an air atmosphere, the gel-state fibres which mainly consist of metal-acetate (M-Ac) and PVP, possibly are subjected to two forces in opposite directions (top left); one is the inward contraction force (σ_i) by pyrolysis of organic components, and the other is the outward adhesive force (σ_o) by rapid out-diffusion of internal gaseous products (such as CO_x, NO_y, and H_2O) due to combustion reactions between the decomposed organic substances and the ambient oxygen; the final fibre morphology depends on the heating rate (*R*) upon calcination; a high *R* results in single-wall hollow fibres composed of large particles (top right), whereas a low *R* leads to fibres featuring double-wall hollow structures with small-sized particles (bottom right).

calcination. On the other hand, the outward force (σ_o) is induced by adhesive, rapid out-diffusion of internal gaseous products (such as CO_x, NO_y, and H_2O) due to the combustion reactions between the decomposed organic substances and the ambient oxygen. At the beginning of the calcination, an intermediate, rigid solid-state outer layer could form on the surface due to facile thermal oxidation. Afterwards, the final fibre morphology would be dependent on the *R* during calcination, affecting the kinetics of the combustion reactions. A high *R* causes fast combustion, and hence, rapid gas out-diffusion ($\sigma_i \ll \sigma_o$), resulting in single-wall hollow fibres composed of large-sized particles, due to the Ostwald ripening (top right), whereas a low *R* induces slow combustion, and hence, consecutive gas out-diffusion and contraction of the gel phase ($\sigma_i > \sigma_o \rightarrow \sigma_i' < \sigma_o'$), giving the fibres a double-wall hollow morphology with small-sized particles (bottom right). In contrast to the formation process of hollow structures by heterogeneous contraction,[13,17] in which a high *R* results in high complexity in the final hollow morphology, the electrospun fibres subjected to a low *R* (0.5 °C/min) in this study showed rather higher complexity than the sample calcined at a high *R* (5 °C/min). This trend was attributed to highly exothermic oxygen-mediated combustion reactions that applied strong, rapid σ_o to gel-state fibres during calcination, in which a low *R* condition could allow sluggish combustion, and hence, repeated release of gaseous products and contraction, resulting in hollow fibres with rather complex interior structures, as demonstrated in Fig. 3.

To investigate one of the applicable electrochemical energy storage fields, we evaluated the lithium storage capability of hollow mesoporous MCO and CMO fibres as anode materials for LIB using 2032 coin-type half-cells. Fig. 5a presents the galvanostatic discharge (Li^+ insertion)–charge (Li^+ extraction) voltage profiles of the MCO-5 and CMO-5 anodes during the first three cycles within a voltage window of 0.01 to 3.0 V (*vs.* Li/Li^+) at a constant current density of 0.1C, where 1C was set at 1000 mA/g. The MCO anode

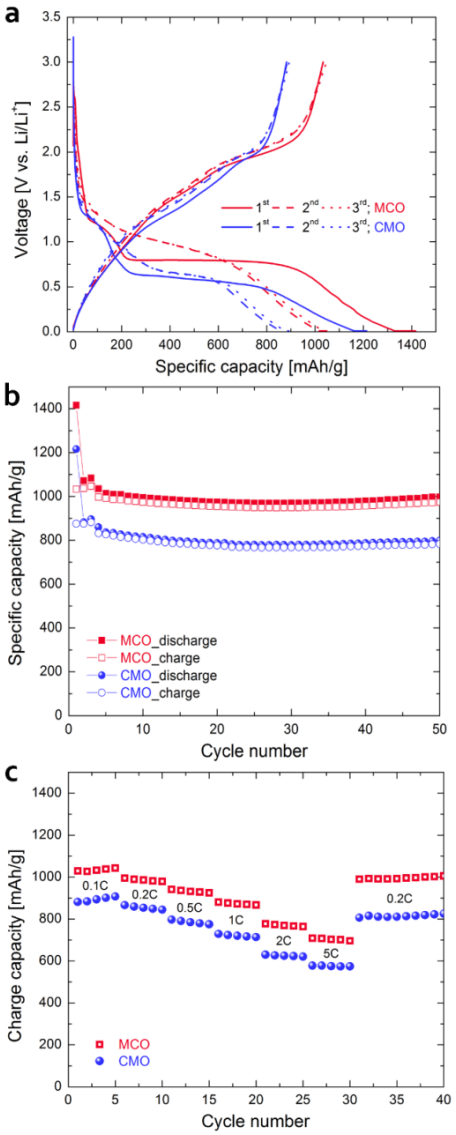

Fig. 5 Electrochemical performance of MCO-5 and CMO-5 fibres anodes. (a) Galvanostatic charge-discharge profiles in the first, second, and third cycles at a constant current density of 0.1 C, (b) cyclability at 0.2 C, and (c) rate capability at 0.1 C–5 C; 1 C was set at 1000 mA/g.

showed the initial discharge and charge capacities of 1402 mAh/g and 1029 mAh/g, respectively, whereas the CMO anode delivered the initial discharge and charge capacities of 1213 mAh/g and 882 mAh/g, respectively, with the initial coulombic efficiency estimated to be 73.4% for the MCO and 72.7% for the CMO. The higher initial discharge capacity compared to the theoretical value (906 mAh/g for MCO and 921 mAh/g for CMO), as shown in the differential capacity plots and eqn (1) and (3) in Fig. S8†, could be attributed to the mesoporous hollow structure of the fibres and the solid-electrolyte interphase (SEI) layer formation.[13,23] Also, the latter may contribute mainly to the initial charge consumption leading to the irreversible capacity loss in the first cycle.[13] Compared to the capacity of the CMO anode, the higher capacity of the MCO anode appeared to be a result of the uniform, small particle size and the relatively large surface area of the MCO fibres, as evidenced by FESEM, TEM, and N_2 sorption analyses.

Next, the cycling performance and rate capability of both anodes were further examined, as shown in Fig. 5b and c. The cells were cycled at a constant current density of 0.2 C in the given operating voltage range for 50 cycles after the initial 3 cycles (at 0.1 C). Even after 50 cycles, the discharge capacity of the MCO and CMO anodes was retained at 997 mAh/g and 798 mAh/g, respectively (Fig. 5b). The Coulombic efficiency during the 50 cycles after the initial cycle reached approximately 98% and 99% for the MCO and CMO anodes, respectively (Fig. S8c†). In addition, both anodes manifested good charge capacity retention at various current densities of 0.1 C–5 C (Fig. 5c). At the high current density of 5 C, the charge capacity of the MCO and CMO anodes was estimated to be 696 mAh/g and 575 mAh/g, respectively. These findings demonstrate that the mesoporous hollow MCO and CMO fibres endowed the anodes with excellent electrochemical properties, such as high lithium storage capability and robust cycling performance and rate capability, which were attributed to the large surface area, as well as the void space stemming from the hollow morphology, leading to enlarged active sites for Li^+ storage and facile Li^+ transportation during cycles.[10,11,24]

In summary, mesoporous hollow MCO and CMO fibres were fabricated by an electrospinning method and highly exothermic combustion reactions via calcination in air. We found that the strong oxygen-mediated combustion reactions within the gel-state fibres gave the fibres hollow structures; the high *R* condition caused abrupt out-diffusion of the gaseous products, resulting in a single-wall tubular morphology, while the low *R* gave rise to a double-wall structure due to consecutive gas out-diffusion and contraction of the gel phase. The electrochemical testing of the MCO and CMO fibres verified their excellent performance for LIB anodes, such as high lithium storage capability, and good cycling stability and rate capability. Furthermore, we considered the possibility of the complete phase formation of MCO and CMO fibres at low synthesis temperatures below 300 ^oC through thermal analyses (Fig. 2). The additional investigation of MCO fibres annealed at 300 ^oC (with *R* of 5 ^oC/min) revealed that the fibres had a hollow morphology and mesoporosity ($S_{BET} \approx 24.1$ m^2/g), but consisted of a mixture of cubic Co_3O_4 and tetragonal $CoMn_2O_4$ phases (refer to Fig. S9†), which require further study for future work.

Acknowledgements

This work was supported by the Energy Efficiency & Resources Core Technology Program of the Korea Institute of Energy Technology Evaluation and Planning (KETEP) granted financial resource from the Ministry of Trade, Industry & Energy, Republic of Korea (No. 20132020000260).

Notes and references

[a]*Institute for Superconducting and Electronic Materials, University of Wollongong, North Wollongong, NSW 2500, Australia. Email: jhk@uow.edu.au*
[b]*Advanced Batteries Research Center, Korea Electronics Technology Institute, Seongnam-si, Gyeonggi-do 463-816, Republic of Korea. Email: parkms@keti.re.kr*
[c]*Department of Advanced Chemicals & Engineering, Chonnam National University, Gwangju 500-757, Republic of Korea*
[d]*New and Renewable Energy Research Division, Korea Institute of Energy Research, Daejeon 305-343, Republic of Korea*
[e]*Department of Physics and Astronomy, College of Science, King Saud University, P.O. Box 2455, Riyadh 11451, Saudi Arabia*
[f]*World Premier International (WPI) Research Center for Materials Nanoarchitectonics (MANA), National Institute for Materials Science (NIMS), Ibaraki 305-0044, Japan*

† Electronic supplementary information (ESI) available: Experimental section; additional thermal analyses, XRD patterns; SEM and TEM results; N_2 adsorption isotherms; differential capacity plots of galvanostatic voltage profiles and coulombic efficiency during cycling. See DOI: 10.1039/c000000x/

‡ These authors contributed equally to this work.

§ Present address: School of Energy and Chemical Engineering, Ulsan National Institute of Science and Technology (UNIST), Ulsan 690-798, Republic of Korea.

1 J.-H. Lee, *Sens. Actuators B: Chem.*, 2009, **140**, 319.
2 A. Walcarius, *Chem. Soc. Rev.*, 2013, **42**, 4098.
3 J. Jiang, Y. Li, J. Liu, X. Huang, C. Yuan and X. W. Lou, *Adv. Mater.*, 2012, **24**, 5166.
4 X. Lai, J. E. Halpert and D. Wang, *Energy Environ. Sci.*, 2012, **5**, 5604.
5 X. Chen, C. Li, M. Grätzel, R. Kostecki and S. S. Mao, *Chem. Soc. Rev.*, 2012, **41**, 7909.
6 S. M. Hwang, Y.-G. Lim, J.-G. Kim, Y.-U. Heo, J. H. Lim, Y. Yamauchi, M.-S. Park, Y.-J. Kim, S. X. Dou and J. H. Kim, *Nano Energy*, 2014, **10**, 53.
7 G. Jeong, J.-G. Kim, M.-S. Park, M. Seo, S. M. Hwang, Y.-U. Kim, Y.-J. Kim, J. H. Kim and S. X. Dou, *ACS Nano*, 2014, **8**, 2977.
8 W Chaikittisilp, K Ariga and Y Yamauchi, *J. Mater. Chem. A*, 2013, **1**, 14.
9 H. Wang, D. Ma, X. Huang, Y. Huang and X. Zhang, *Sci. Rep.*, 2012, 2, 701.
10 C. Yuan, H. B. Wu, Y. Xie and X. W. Lou, *Angew. Chem. Int. Ed.*, 2014, **53**, 1488.
11 P. Simon, Y. Gogotsi and B. Dunn, *Science*, 2014, **343**, 1210.
12 F. Cheng, J Shen, B. Peng, Y. Pan, Z. Tao and J. Chen, *Nat. Chem.*, 2011, **3**, 79.
13 L. Zhou, D. Zhao and X. W. Lou, *Adv. Mater.*, 2012, **24**, 745.
14 G. Zhang and X. W. Lou, *Adv. Mater.*, 2013, **25**, 976.
15 K.-N. Jung, S. M. Hwang, M.-S. Park, K. J. Kim, J.-G. Kim, S. X. Dou, J. H. Kim and J.-W. Lee, *Sci. Rep.*, 2015, **5**, 7655.
16 Y. Xu, X. Wang, C. An, Y. Wang, L. Jiao and H. Yuan, *J. Mater. Chem. A*, 2014, **2**, 16480.
17 J. Guan, F. Mou, Z. Sun and W. Shi, *Chem. Commun.*, 2010, **46**, 6605.
18 D.-K. Kwon, T. Akiyoshi, H. Lee and M. T. Lanagan, *J. Am. Ceram. Soc.*, 2008, **91**, 906.
19 W. Ponhan and S. Maensiri, *Solid State Sci.*, 2009, **11**, 479.
20 J. Reed and G. Ceder, *Chem. Rev.*, 2004, **104**, 4513.
21 W. Wei, W. Chen and D. G. Ivey, *Chem. Mater.*, 2008, **20**, 1941.
22 M. Kruk and M. Jaroniec, *Chem. Mater.*, 2001, **13**, 3169.
23 Z.-S. Wu, W. Ren, L. Wen, L. Gao, J. Zhao, Z. Chen, G. Zhou, F. Li and H.-M. Cheng, *ACS Nano*, 2010, **4**, 3187.
24 X. Huang, R. Wang, D. Xu, Z. Wang, H. Wang, J. Xu, Z. Wu, Q. Liu, Y. Zhang and X. Zhang, *Adv. Funct. Mater.*, 2013, 23, 4345.